The Astrophysical Journal, 697:923–933, 2009 May 20 doi:10.1088/0004-637X/697/1/923

TURBULENT DYNAMOS IN SPHERICAL SHELL SEGMENTS OF VARYING GEOMETRICAL EXTENT

Dhrubaditya Mitra[1], Reza Tavakol[1], Axel Brandenburg[2], and David Moss[3]
[1] Astronomy Unit, School of Mathematical Sciences, Queen Mary University of London, Mile End Road, London E1 4NS, UK; dhruba.mitra@gmail.com
[2] NORDITA, Roslagstullsbacken 23, SE-10691 Stockholm, Sweden; brandenb@nordita.org
[3] School of Mathematics, University of Manchester, Oxford Road, Manchester M13 9PL, UK; David.Moss@manchester.ac.uk
Received 2008 December 16; accepted 2009 March 5; published 2009 May 5

ABSTRACT

We use three-dimensional direct numerical simulations of the helically forced magnetohydrodynamic equations in spherical shell segments in order to study the effects of changes in the geometrical shape and size of the domain on the growth and saturation of large-scale magnetic fields. We inject kinetic energy along with kinetic helicity in spherical domains via helical forcing using Chandrasekhar–Kendall functions. We take perfect conductor boundary conditions for the magnetic field to ensure that no magnetic helicity escapes the domain boundaries. We find dynamo action giving rise to magnetic fields at scales larger than the characteristic scale of the forcing. The magnetic energy exceeds the kinetic energy over dissipative timescales, similar to that seen earlier in Cartesian simulations in periodic boxes. As we increase the size of the domain in the azimuthal direction, we find that the nonlinearly saturated magnetic field organizes itself in long-lived cellular structures with aspect ratios close to unity. These structures tile the domain along the azimuthal direction, thus resulting in very small longitudinally averaged magnetic fields for large domain sizes. The scales of these structures are determined by the smallest scales of the domain, which in our simulations is usually the radial scale. We also find that increasing the meridional extent of the domains produces little qualitative change, except a marginal increase in the large-scale field. We obtain qualitatively similar results in Cartesian domains with similar aspect ratios.

Key words: MHD – turbulence

Online-only material: color figures

1. INTRODUCTION

A fundamental question in solar and stellar physics concerns the generation of large-scale magnetic fields in convective spherical shells through dynamo action, which occurs on dynamical timescales. A great deal of effort has gone into understanding this question by using direct three-dimensional magnetohydrodynamic (MHD) simulations, in Cartesian domains with forced and convective turbulence as well as in spherical domains. These studies can be divided into four broad groups. The first consists of helically forced turbulence simulations in Cartesian domains, see, e.g., Brandenburg (2001) and Brandenburg & Dobler (2001). These simulations in general show large-scale magnetic fields when periodic or perfect conductor boundary conditions are used, but only growing on dissipative timescales, which makes them not directly relevant to solar and stellar situations. With more realistic open boundary conditions and in the presence of shear, large-scale magnetic fields are known to develop on dynamical timescales (Brandenburg 2005). The second group comprises simulations of turbulent convection in Cartesian coordinates, which have recently shown large-scale magnetic fields (Käpylä et al. 2008; Hughes & Proctor 2008). Third, forced incompressible turbulence simulations in full spheres, mostly relevant to planetary dynamos, have been carried out by Mininni & Montgomery (2006) and Mininni et al. (2007). Finally, there is an increasing body of work employing simulations of MHD turbulence in spherical rotating shells with convection using the incompressibility constraint with either Boussinesq approximations (Gilman & Miller 1981; Gilman 1983) or anelastic approximations (Gilman & Glatzmaier 1981; Glatzmaier & Gilman 1982; Glatzmaier 1984, 1985; Miesch et al. 2000; Brun et al. 2002, 2004, 2006; Brown et al. 2007). These simulations produce mainly small-scale magnetic fields and only insignificant large-scale magnetic fields with parameters relevant to the solar and stellar settings. Relatively stronger large-scale (global) magnetic fields have, however, been found in rapidly rotating shells (Brown et al. 2007). Also, it has recently been shown that in simulations of fully convective stars the energy in the longitudinally averaged magnetic field can become locally comparable to the kinetic energy (Browning 2008).

In the present paper, we attempt to bridge the gap between studies in Cartesian and spherical shell domains by solving the MHD equations in wedge-shaped domains of spherical shells with helical forcing. In particular, we study the effects of shape and size of the computational domain on the growth and saturation of the large-scale magnetic field. Spherical-wedge geometries, in principle, provide an advantage in terms of computational resources over both the Cartesian boxes and spherical shell geometries usually employed in MHD simulations in that they strike a reasonable compromise between the requirements for spatial resolution and globality. In other words, our choice of spherical wedge domains allows in principle higher absolute spatial resolution (i.e., higher number of grid points per unit length), thus potentially allowing larger magnetic Reynolds numbers (defined later) to be attained, while retaining some globality. Alternatively, at a given resolution, we can achieve simulations in a number of wedge domains, or in one domain for much longer time, for the cost of one simulation in a full spherical shell—this is the approach we adopt here.

In this paper, we make a number of assumptions that are motivated by the desire to understand the basic concepts of dynamo saturation in spherical geometries instead of providing a realistic model of the solar dynamo. Specifically, we consider here the case of homogeneous turbulence with perfectly conducting boundary conditions so as to make contact with corresponding

earlier work in Cartesian domains. The physically more relevant case of open boundary conditions with an equator and differential rotation or shear will be postponed to future work.

The paper is organized as follows. In Section 2, we briefly describe the details of our model and the code used. Section 3 contains our results, where for the sake of clarity, we present the results concerning the effects of increasing the domain in the azimuthal and meridional directions separately. Section 4 contains our conclusions. Finally, Appendices A and B contain the details of the helical forcing used, and our extension of the Pencil Code[4] to non-Cartesian coordinate systems, respectively.

2. THE MODEL

We solve numerically the MHD equations for the velocity $\boldsymbol{U}$, the logarithmic density $\ln \rho$, and the vector potential $\boldsymbol{A}$, given by

$$D_t \boldsymbol{U} = -c_s^2 \boldsymbol{\nabla} \ln \rho + \frac{1}{\rho} \boldsymbol{J} \times \boldsymbol{B} + \boldsymbol{F}_{\rm visc} + \boldsymbol{f}, \quad (1)$$

$$D_t \ln \rho = -\boldsymbol{\nabla} \cdot \boldsymbol{U}, \quad (2)$$

$$\partial_t \boldsymbol{A} = \boldsymbol{U} \times \boldsymbol{B} + \eta \nabla^2 \boldsymbol{A}, \quad (3)$$

where $\boldsymbol{F}_{\rm visc} = (\mu/\rho)\left(\nabla^2 \boldsymbol{U} + \frac{1}{3} \boldsymbol{\nabla} \boldsymbol{\nabla} \cdot \boldsymbol{U}\right)$ is the viscous force, μ is the dynamic viscosity, $\boldsymbol{B} = \boldsymbol{\nabla} \times \boldsymbol{A}$ is the magnetic field, $\boldsymbol{J} = \boldsymbol{\nabla} \times \boldsymbol{B}/\mu_0$ is the current density, μ_0 is the vacuum permeability, c_s^2 is the velocity of sound in the medium, ρ is the density, η is the magnetic diffusivity, and $D_t \equiv \partial_t + \boldsymbol{U} \cdot \boldsymbol{\nabla}$ is the advective derivative. Here, $\boldsymbol{f}(\boldsymbol{x}, t)$ is an external random helical forcing (the details of which are given in Appendix A), satisfying the condition

$$\boldsymbol{f} \cdot \boldsymbol{\nabla} \times \boldsymbol{f} \geqslant 0, \quad (4)$$

in order to ensure positive helicity injection over the entire sphere. Such a model is reminiscent of constant α effect spheres that were studied in the early days of mean-field dynamo theory (Krause & Steenbeck 1967). Similar cases relevant to planetary dynamos have also been studied recently by direct numerical simulations (Mininni & Montgomery 2006; Mininni et al. 2007).

A sketch of the meridional cross-section of a typical wedge-shaped domain used in our simulations is given in Figure 1. We confine ourselves to simulations in the northern hemisphere. However, because there is no rotation, the choice of the coordinate axis (and hence of the equator) is arbitrary. Therefore, the physical conditions are the same on either side of the equator. The code used for our computations is the Pencil Code developed by Brandenburg & Dobler (2002) in Cartesian coordinates. We have extended the code to allow simulations in spherical coordinates. This was facilitated by the fact that the Pencil Code was already written in a nonconservative form, which allowed the curvilinear coordinates to be implemented by replacing all partial derivatives by covariant derivatives, see Appendix B for further details.

Guided by the convection zone of the Sun, in the majority of our computations the radial extent of our domain is chosen to be $0.7 \leqslant r \leqslant 1.0$. We use perfect conductor boundary conditions for the magnetic field to ensure that no magnetic helicity escapes the domain boundaries. In Cartesian domains (Brandenburg 2001), this is often achieved by assuming periodic boundary conditions across the boundaries. In our spherical case, this translates to the normal component of the magnetic field $\boldsymbol{B}$ being continuous (and hence zero) across the boundary. This implies that the tangential components of the magnetic vector potential $\boldsymbol{A}$ must be zero at the boundary. We are free to choose the boundary condition for the normal component. Guided by this, we make the following choices at the four boundaries of our domain:

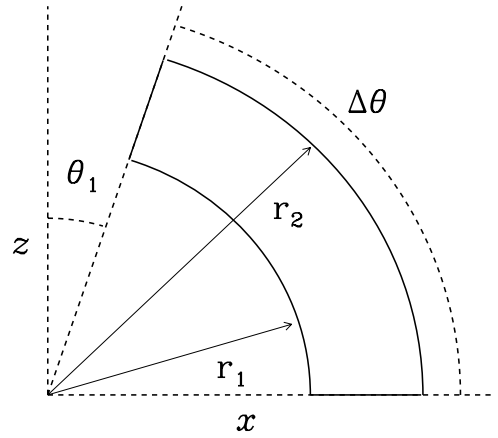

Figure 1. Schematic representation of the meridional plane of our spherical wedge computational domain. We also define θ_2 to be the angle that the other azimuthal boundary makes with the polar axis; in this figure and throughout this paper, $\theta_2 = \pi/2$.

$$A_\theta = A_\phi = \frac{dA_r}{dr} = 0 \quad (\text{on } r = r_1), \quad (5)$$

$$A_\theta = A_\phi = A_r = 0 \quad (\text{on } r = r_2 \text{ and } \theta = \theta_2 = \pi/2), \quad (6)$$

$$A_r = A_\phi = \frac{dA_\theta}{d\theta} = 0 \quad (\text{on } \theta = \theta_1). \quad (7)$$

There is no particular reason for using $A_r = 0$ on $r = r_2$ and not on $r = r_1$, and we emphasize that the condition on the normal component of $\boldsymbol{A}$ is of no significance for $\boldsymbol{B}$ itself. We use stress-free boundary conditions for the velocity at all these four boundaries and periodic boundary conditions for all the variables along the azimuthal direction.

3. RESULTS

Our principle aim in this paper is to study the growth and saturation of large-scale magnetic field in spherical wedge domains. In particular, we study the effects of changes in the shape and size of the domain on the resulting large-scale fields. For the sake of clarity, we do this by studying the effects of increasing the domain extent in the θ and ϕ directions in turn. We also briefly look at the role of the radial extent of the computational domain. Given that the size of our simulation domain is different along different directions in different runs, we in general have three different length scales, $L_r \equiv r_2 - r_1$, $L_\theta \equiv r_2(\theta_2 - \theta_1)$, and $L_\phi \equiv r_2 \sin\theta_2(\phi_2 - \phi_1)$, corresponding to the sizes of the domain in the r, θ, and ϕ directions, respectively. As an estimate of the characteristic Fourier mode of forcing, we use $k_{\rm f} = W_{\rm rms}/U_{\rm rms}$, where $W_{\rm rms} = \langle \boldsymbol{W}^2 \rangle^{1/2}$ is the rms value of the vorticity, $\boldsymbol{W} \equiv \nabla \times \boldsymbol{U}$, and $U_{\rm rms}$ is the rms velocity. Here, angular brackets denote volume averages. The characteristic length scale of forcing is defined to be $\ell_{\rm f} \equiv 2\pi/k_{\rm f}$. We then define the fluid Reynolds number, magnetic Reynolds number,

[4] http://www.nordita.org/software/pencil-code.

Table 1
Parameters of the Spherical Runs

Runs	Grid	L_θ	L_ϕ	ℓ_f/L_r	Re	$\mathrm{Re_M}$	H_K	λ
S1	$32\times32\times32$	0.1π	0.1π	0.5	5	14	0.66	0.08
S2	$32\times32\times128$	0.1π	$\pi/2$	0.4	5	12	0.74	0.10
S3	$32\times32\times256$	0.1π	π	0.4	5	12	0.74	0.10
S4	$32\times64\times32$	0.2π	0.10π	0.5	5	12	0.65	0.10
S5	$32\times256\times32$	85°	0.1π	0.4	5	12	0.73	0.14
S6	$32\times64\times128$	0.2π	$\pi/2$	0.4	5	11	0.79	0.10
S7	$32\times32\times64$	0.1π	$\pi/4$	0.2	2	4	0.79	0.10

and the turnover time as $\mathrm{Re} = U_{\rm rms}/\nu k_f$, $\mathrm{Re_M} = U_{\rm rms}/\eta k_f$, and $\tau \equiv (U_{\rm rms}k_f)^{-1}$, respectively. Here, ν is the kinematic viscosity given by $\nu = \mu/\rho_0$ where ρ_0 is the initial density (which is equal to the mean density throughout, noting that the mass in the volume is conserved). In all our runs τ is nearly the same and varies from $0.6c_s/r_2$ (run S7) to $0.9c_s/r_2$ (run S1). As the dynamo we study is resistively limited (e.g., Brandenburg 2001), the timescale of saturation is the dissipative timescale $\tau_\eta = \eta k_1^2$ which is used to nondimensionalize the time. $\tau_\eta = \eta k_1^2$ which we use to normalize the time axes of our plots. Here, k_1 is the wavenumber corresponding to the smallest length scale in our domain, i.e., $k_1 \equiv 2\pi/L_r$ for most of our runs. The helical nature of the velocity field is characterized by $H_K = \langle \boldsymbol{W}\cdot\boldsymbol{U}\rangle/(W_{\rm rms}U_{\rm rms})$. We start our simulations with a zero velocity field and a Gaussian random magnetic vector potential such that the amplitude of the magnetic field is of the order of 10^{-6} in units of $(\rho_0\mu_0)^{1/2}c_s$.

The growth and saturation of the magnetic dynamo is monitored by the total magnetic energy, $E_M = \langle \boldsymbol{B}^2\rangle/2\mu_0$, and the kinetic energy, $E_K = \langle \rho \boldsymbol{U}^2\rangle/2$. We define the large-scale (or mean) magnetic field using longitudinal averaging,

$$\overline{\mathbf{B}}(r,\theta,t) \equiv \frac{1}{2\pi}\int \boldsymbol{B}\, \mathrm{d}\phi, \tag{8}$$

over the extent of the domain. The total energy in the large-scale magnetic field is then defined by $E_{\rm LS}(t) = \langle \overline{\boldsymbol{B}}^2\rangle/2\mu_0$.

A measure of the level of turbulence in our simulations is the Reynolds number, Re, given in Table 1, which is about 5 in all the runs except run S7 in which case it is 2. For all practical purposes, there is essentially no inertial range in the spectrum of the fluid obtained from our runs.

The summary of the runs together with their domain sizes, resolutions, and other relevant parameters are given in Table 1. In the following subsections, we summarize the results of our simulations as the domain sizes in the azimuthal and meridional directions, L_ϕ and L_θ, respectively, are changed separately.

3.1. Initial Growth Phase

We first summarize our results concerning the growth phase of the dynamos. We begin with the run with the smallest domain size, i.e., S1; see Figure 2. As can be seen the magnetic energy starts growing exponentially from $t \approx 0.2\tau_\eta$ and the total magnetic energy reaches the level of the kinetic energy at $t \approx 3\tau_\eta$. This is true of all our runs, since they all start with the same initial field strength, and they all have the same growth rate which, in turn, is proportional to $U_{\rm rms}k_f$, which is also the same for all runs. The growth rate during this exponential growth phase is given by

$$\lambda(t) = \frac{\mathrm{d}}{\mathrm{d}t}\ln\langle \boldsymbol{B}^2\rangle_{\rm lin}^{1/2}, \tag{9}$$

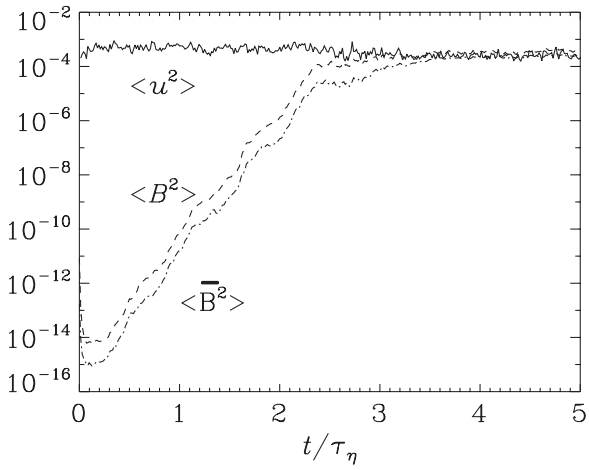

Figure 2. Evolution of $\langle \boldsymbol{U}^2\rangle$ (continuous), $\langle \boldsymbol{B}^2\rangle$ (dashed), and $\langle \overline{\boldsymbol{B}}^2\rangle$ (dash-dotted) during early times from run S1. Similar exponential growth of the magnetic energy is seen in all the other runs.

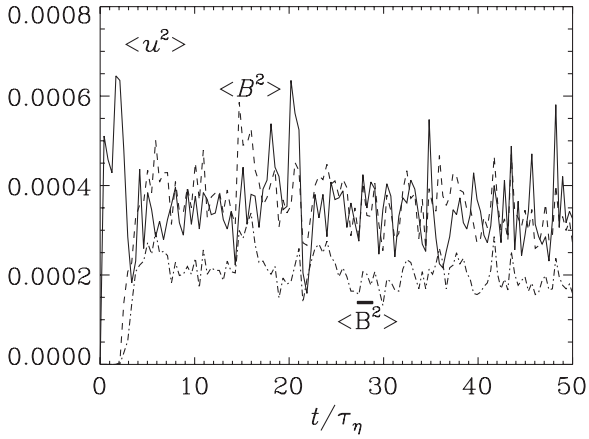

Figure 3. Evolution of kinetic energy $\langle \boldsymbol{U}^2\rangle$ (continuous), magnetic energy $\langle \boldsymbol{B}^2\rangle$ (dashed), and energy in the large-scale magnetic field $\langle \overline{\boldsymbol{B}}^2\rangle$ (dash-dotted) during late times from run S1. The saturated value of the energy in the large-scale magnetic field is comparable to the kinetic energy.

which is about 0.1 for all the runs performed here; see Table 1. In all cases, E_K decreases (i.e., it is quenched) after E_M reaches saturation. We note that even after reaching saturation the field keeps growing somewhat, similar to what has been seen earlier in Cartesian domains with periodic boundary conditions (Brandenburg 2001), or with perfectly conducting boundaries (Brandenburg & Dobler 2002). Both E_K and H_K decrease slightly (by less than 10%) after saturation is reached for runs S2, S3, and S6. For other runs the H_K decreases a little more (by factors from about 0.8 to 0.6).

3.2. Formation of Large-Scale Magnetic Field

For the smallest domain chosen here, i.e., S1 which is closest to a cube ($L_r \approx L_\theta \approx L_\phi$), we obtain results that are very similar to those found earlier from Cartesian simulations (Brandenburg 2001). The large-scale magnetic field grows, reaches a value close to equipartition, and then shows a slow saturation on dissipative timescales, see Figure 3. As we are using perfectly conducting boundary conditions, the growth of the large-scale magnetic field is limited by the decay of small-scale magnetic helicity. This has been used to model the saturation of the magnetic energy of the large-scale field (Brandenburg 2001),

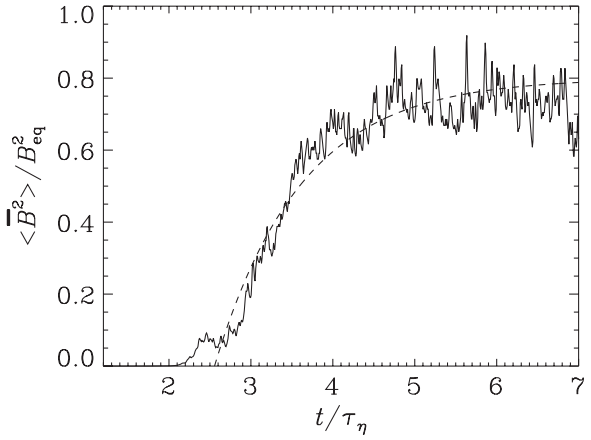

Figure 4. Late saturation behavior of the mean field $\overline{\boldsymbol{B}}$ for the run S1 compared to the prediction given by Equation (10) (dashed).

$$\frac{\overline{B}^2}{B_{\rm eq}^2} = \frac{\epsilon_{\rm f} k_{\rm f}}{\epsilon_{\rm m} k_{\rm m}} [1 - e^{-2\eta k_m^2 (t - t_{\rm sat})}]. \tag{10}$$

Here, $t_{\rm sat}$ is the approximate time when the small-scale field has saturated, and k_m is a new effective wavenumber which is related to k_1 and is treated here as a fit parameter that is chosen to match the simulation result. We obtain $k_m \approx 0.7 k_1$. Here, $B_{\rm eq}^2$ corresponds to the kinetic energy density, so $B_{\rm eq}^2/\mu_0 = \langle \rho u^2 \rangle$, and is approximately equal to the energy in the small-scale magnetic field. Expression (10) fits the data from our simulations quite well as shown in Figure 4.

The evolution of the large-scale magnetic field follows closely the evolution of the total magnetic field after the time when the amplitude of the large-scale field has become steady. The growth of large-scale structures for this run (run S1) in the equatorial plane and the meridional plane are shown in Figures 5 and 6, respectively. Large-scale structures in the contour plots of magnetic field in the equatorial plane appear as early as $t \approx 500$ (about $6\tau_\eta$) and at late times they encompass the whole azimuthal extent of the domain.

3.3. Effects of Increasing the Azimuthal Extent

To proceed, we begin by increasing the domain size in the ϕ direction, while keeping the θ and r dimensions fixed, and increase thereby the aspect ratio. The initial growth phase remains practically unchanged as we change the extent of our domain. We find that the large-scale magnetic field decreases as we go to larger domains (by increasing L_ϕ), as can be seen in Figure 7.

To understand the reason for this decrease in the large-scale magnetic field, we present contour plots of the θ component of magnetic field in the equatorial plane for four different domain sizes at later times (see Figure 8). Note that as we increase our domain size "cell-like" structures are developed along the azimuthal direction, with aspect ratios close to unity. Their typical length scale corresponds to and seems to be determined by the smallest dimension of our domain, which here is the radial extent. We checked this by performing a run with half the radial extent and found that the characteristic horizontal scale of the cell structures is decreased accordingly, to half the original value. We also find that the length scale of these cell structures does not depend on the forcing length scale. We verified this by changing the forcing length scale along the radial direction and found that this does not change these cell structures. The length scale of the cells is also larger than the characteristic length scale of the velocity. This is best described using Fourier transform along the azimuthal (periodic) direction,

$$\hat{\boldsymbol{U}}_m(r,\theta) = \int \boldsymbol{U}(r,\theta,\phi) \exp(im\phi) \frac{{\rm d}\phi}{2\pi}, \tag{11}$$

$$\hat{\boldsymbol{B}}_m(r,\theta) = \int \boldsymbol{B}(r,\theta,\phi) \exp(im\phi) \frac{{\rm d}\phi}{2\pi}. \tag{12}$$

We can define the averaged spectra of these Fourier-transformed quantities as

$$S_m^{\rm U} = \langle |\hat{\boldsymbol{U}}_m(r,\theta)|^2 \rangle_{r\theta}, \qquad S_m^{\rm B} = \langle |\hat{\boldsymbol{B}}_m(r,\theta)|^2 \rangle_{r\theta}, \tag{13}$$

where the subscript $r\theta$ denotes meridional averaging. Note that $\sum S_m^{\rm U} = \langle \boldsymbol{U}^2 \rangle$ and $\sum S_m^{\rm B} = \langle \boldsymbol{B}^2 \rangle$. We plot in Figure 9 both $S_m^{\rm B}$ and $S_m^{\rm U}$ for the runs S1, S2, and S3, which have azimuthal extents $\pi/10$, $\pi/2$, and π, respectively. We find that the peak in the spectrum of the magnetic field occurs at the same m for runs S2 and S3, showing that the typical characteristic scale of the periodic structures does not depend on the ϕ extent of our domain. Note also that the typical forcing scale is clearly smaller than this (corresponding to $m \approx 20$–40).

An important question regarding these structures, and hence the resulting large-scale magnetic fields, is whether these periodic structures are transient and may later merge to form structures encompassing the whole domain similar to the run S1 with the smallest domain size. The characteristic timescale over which structures encompassing the whole domain form in S1 is about $6\tau_\eta$. In Cartesian simulations with magnetically closed boundaries the saturation time is inversely proportional to the square of the relevant domain size. Thus, by analogy, if the ϕ extent is doubled the timescale $\sim 6\tau_\eta$ would become $\sim 24\tau_\eta$. Similarly, it would take even longer for such structures to form in the runs with bigger domain size. We have studied a run—run S7—in which the azimuthal extent of the domain is twice that of S1 and have run this simulations up to $500\tau_\eta$, without finding any evidence of cells merging. This suggests that the periodic structures that we observe are at least as long-lived as the duration of our longest runs.

To summarize, our simulations show that the characteristic scale of the large-scale magnetic fields found in our simulations is about the scale of the radial extent of our domain. Hence, as we increase L_ϕ an increasing number of periodic structures appear along the azimuthal direction, which, in the largest domain we have used, is about 10 times larger than the radial direction. Therefore the large-scale magnetic field, defined as a longitudinal average, gives a very small contribution in the runs with larger domains. Note that, with this definition, the energy of the large-scale magnetic field corresponds to the energy in the (axisymmetric) S_0^B mode. From the plot of the spectrum we note that most of the magnetic energy is actually concentrated at $m = 8$, which is the scale of a cell, and this mode indeed shows super-equipartition. Also note that this mode corresponds to length scales larger than the scale of forcing, which corresponds to $m \approx 20$–40. Hence, instead of using the longitudinal average to calculate the energy in the large-scale magnetic field we can use the energy in the mode $m = 8$ of the meridionally averaged spectrum of the magnetic field. A comparison between these two methods of calculation of energy in the large-scale magnetic field is shown in Figure 10. Note that as L_ϕ is increased the large-scale magnetic energy measured by the averaged spectrum of the magnetic field remains practically constant.

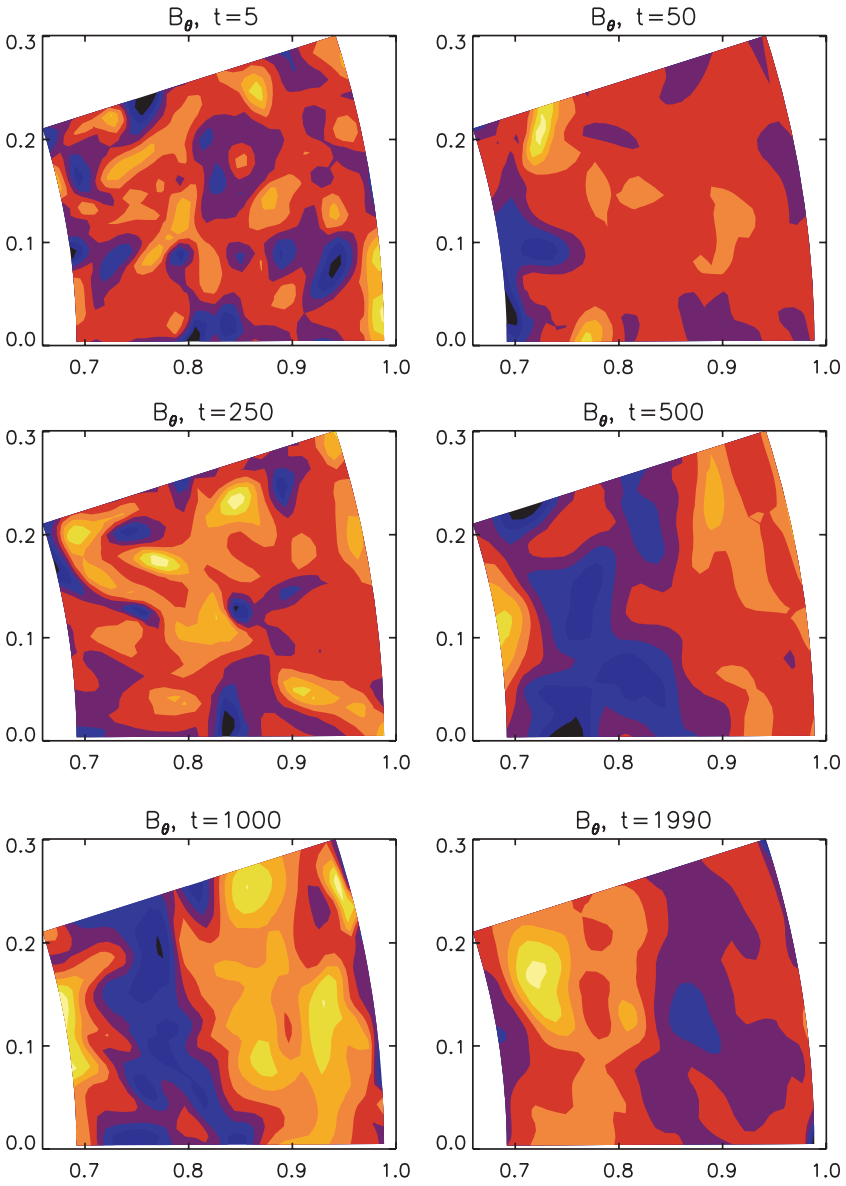

Figure 5. Contour plots of B_θ in the equatorial plane of the domain in S1 at different times showing the gradual establishment of a large-scale magnetic field. Time is here given in units of R/c_s.

(A color version of this figure is available in the online journal.)

3.4. Effects of Increasing the Meridional Extent

Next we study the effects of increasing the domain size by increasing the meridional extent. We find that, as we increase the domain size along the θ direction, the large-scale magnetic field shows marginal increase; see Figure 11. Contour plots of the toroidal component of the magnetic field in the meridional plane for the runs S1, S4, and S5 are shown in Figure 12. Note that, as the domain is increased in the θ direction, the field structure at low latitudes is largely unchanged, while new weaker fields are added at high latitudes. However, the high latitudes contribute relatively little to the volume average, so the magnetic energy is only marginally increased. As noted above, our use of the term high latitudes is defined by our arbitrary choice of the coordinate axis—see Figure 1. However, once such a choice is made, the field can only develop subject to the constraints imposed by the geometry of the computational domain.

Again, we have checked that the characteristic scale of the cells is determined by the smallest of the three dimensions of our domain, by performing a simulation in which the meridional extent of the domain is half that of run S1. We find that the resulting cells again have length scales comparable to the smallest scale of the domain which in this case is the meridional extent. Furthermore, we have checked that, as we increase our domain along the azimuthal extent, the cell-like structures in our simulations are independent of the meridional extent of the domain, provided that the radial scale remains the smallest. To illustrate this we compare contour plots of B_θ in the equatorial plane for the runs S2 and S6 in Figure 13. These two runs have the same azimuthal extent, $L_\phi = \pi/2$, but different meridional extents, viz., $L_\theta = \pi/10$ for the run S2 and $L_\theta = \pi/4$ for the run S6. As can be seen the cell-like structures that appear have the same global features. Finally, we have checked that the characteristic length scale of cells is independent of

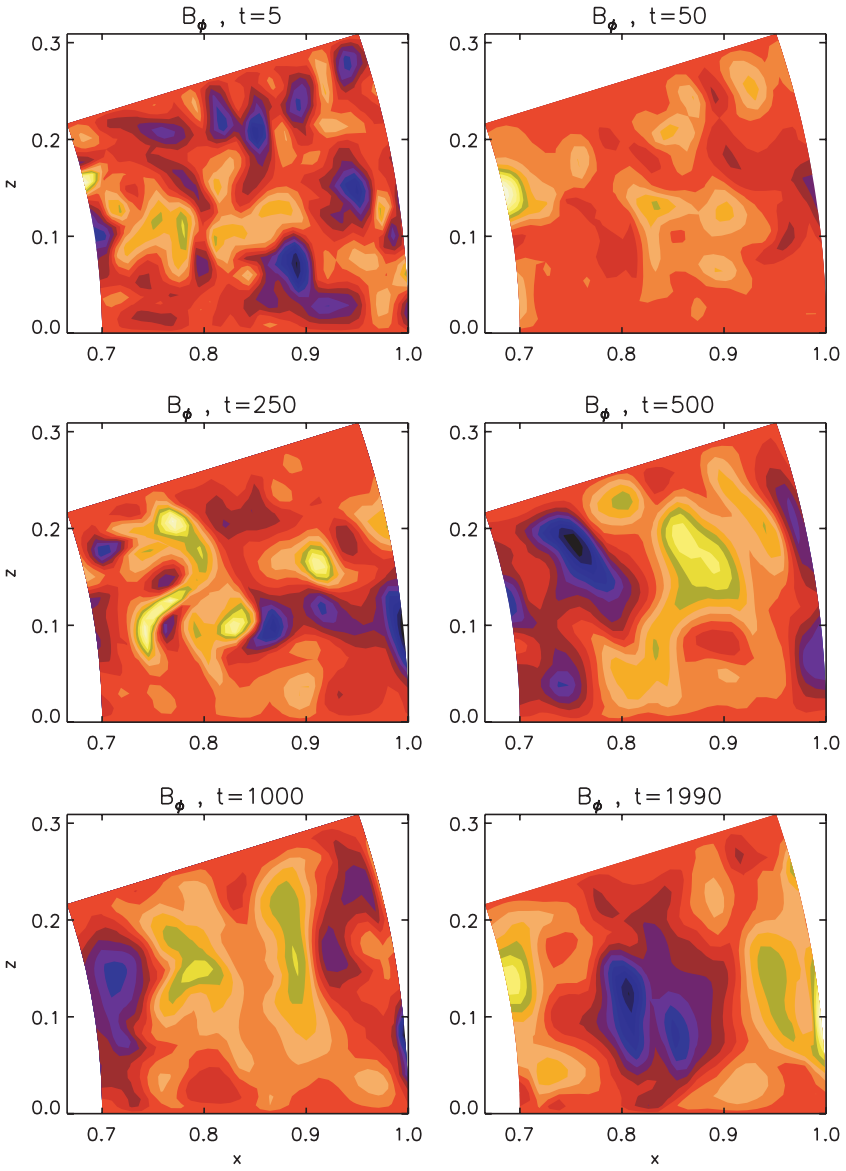

Figure 6. Contour plots of B_ϕ in the meridional plane of the domain in S1 at different time. Time is here given in units of R/c_s.
(A color version of this figure is available in the online journal.)

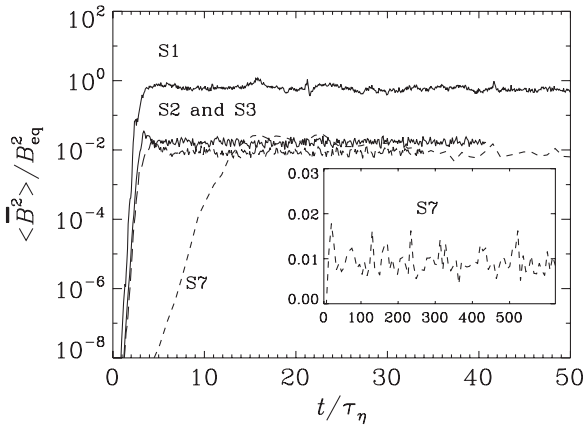

Figure 7. Normalized energy in the large-scale magnetic field vs. time for the runs S1, S2, S3, and S7. As can be seen, as the domain size increases in the ϕ-direction the field decreases (see also Figure 10). The inset shows the same plot but in linear scale for the run S7 which was run more than 10 times longer than the other cases.

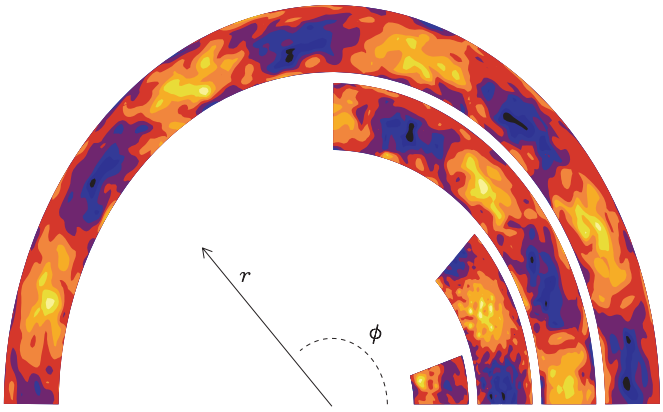

Figure 8. Contour plots showing the typical structure of the magnetic field in the equatorial plane as the ϕ extent of the domain is increased. From top to bottom, plots of the runs S3, S2, S7, and S1.
(A color version of this figure is available in the online journal.)

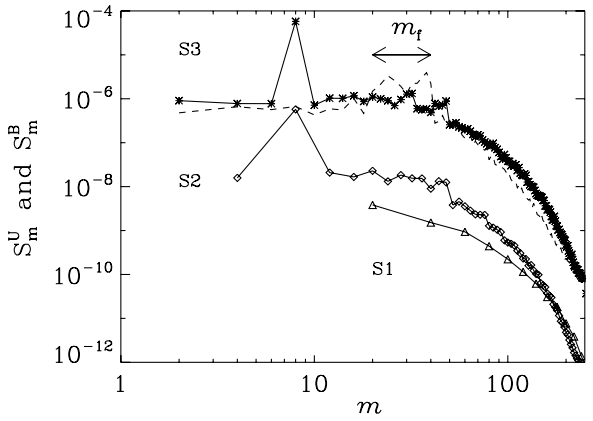

Figure 9. Kinetic and magnetic energy spectra S_m^U (dashed line) and S_m^B (continuous line) from runs S1, S2, and S3. The range of scales being forced are shown within the two arrowheads. For clarity the spectrum for run S1 and S2 are multiplied by a factor of 10^{-4} and 10^{-2}, respectively.

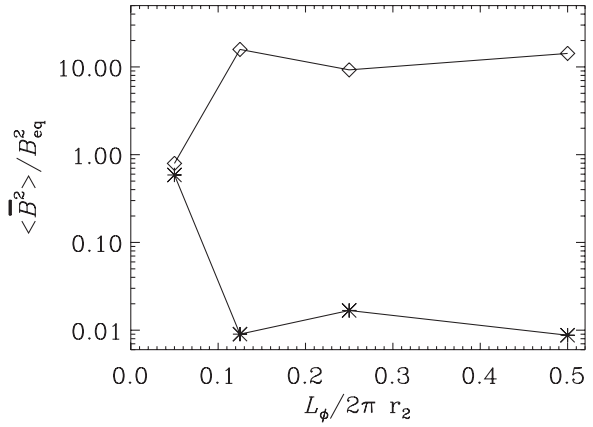

Figure 10. Two different measures to estimate the energy in the large-scale magnetic field plotted against L_ϕ, for four different runs having different domain sizes along the azimuthal direction. In one case, the large-scale magnetic energy is estimated by longitudinal average (denoted by $*$ in the plot), in the other case (denoted by $\diamond$ in the plot) it is estimated by the magnitude of the peak of S_m^B.

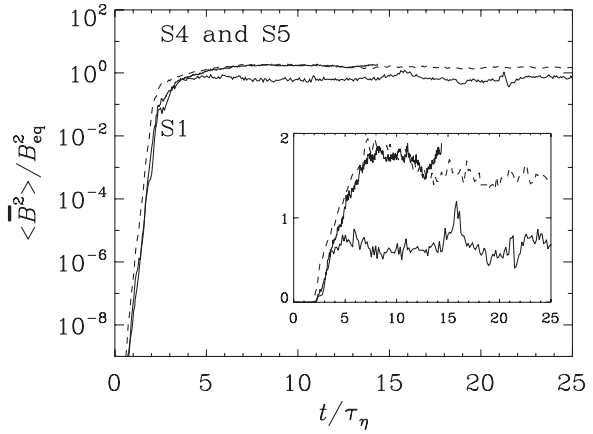

Figure 11. Normalized energy in the large-scale magnetic field vs. time for three different runs S1, S4, and S5. The inset shows the same plot but in linear scale.

the forcing scale by performing a simulation in which the characteristic scale of forcing is half that of the scale of forcing in run S1.

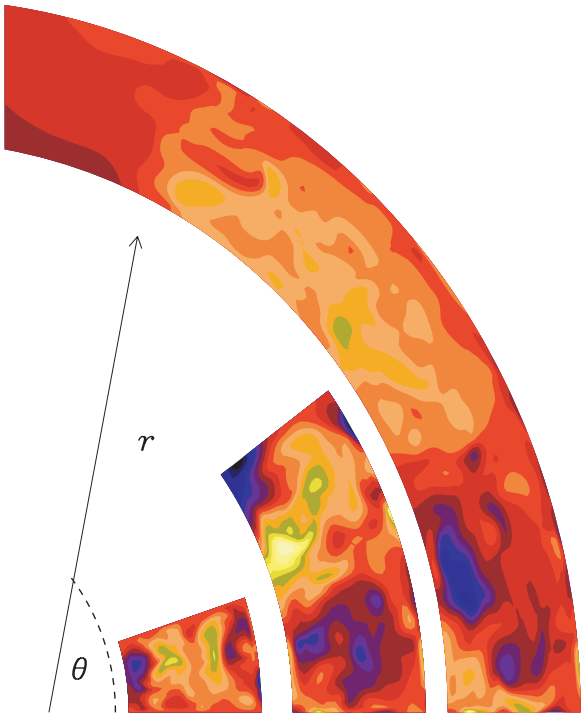

Figure 12. Meridional cross-sections of B_ϕ after saturation has been reached. From left to right: S1, S4, and S5.

(A color version of this figure is available in the online journal.)

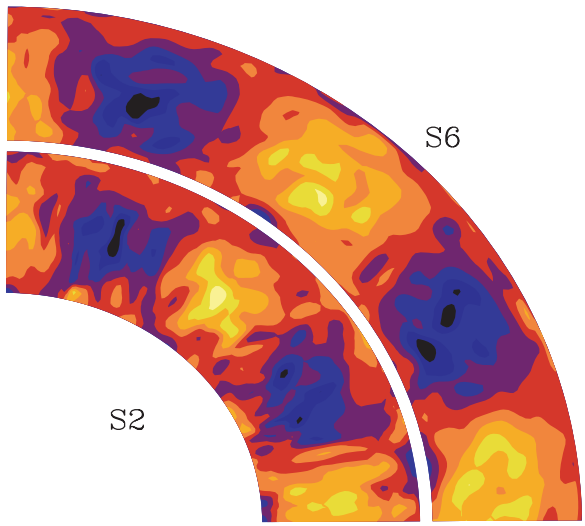

Figure 13. Equatorial cross-sections of B_θ after saturation has been reached from runs S2 and S6.

(A color version of this figure is available in the online journal.)

3.5. Cartesian Versus Spherical: Geometry Versus Aspect Ratio

An important question concerning our results is how to differentiate between the effects of geometry (globality) and changes in the aspect ratio. To answer this question, we need to compare our wedge domain simulations with simulations in Cartesian boxes with appropriate aspect ratios. To this end, we perform two simulations in Cartesian coordinates—runs C1 and C2—with aspect ratios 1 and 2, respectively. Relevant parameters for these runs are summarized in Table 2. These Cartesian simulations correspond to the runs S1 and S7 in the spherical wedge domains. The main features of our spherical runs are also found in the Cartesian runs. In particular, we

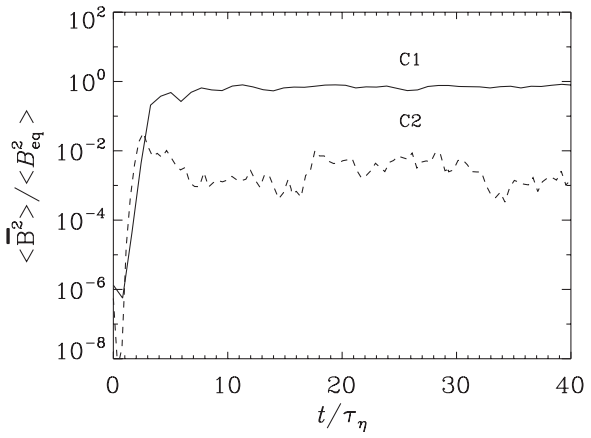

Figure 14. Normalized energy in the large-scale magnetic field vs. time for the runs C1, C2. As can be seen, as the domain size increases in the z-direction, the field decreases in a way very similar to the spherical case.

Table 2
Summary of the Runs, Including the Extents of the Computational Domains for the Cartesian Runs

Runs	Grid	L_y	L_z	ℓ_f/L_x	$\mathrm{Re} = \mathrm{Re_M}$	H_K	τ
C1	$32 \times 32 \times 32$	6	6	0.5	16	0.7	2.6
C2	$32 \times 32 \times 128$	6	12	0.7	25	0.6	3.6

find that the initial (kinematic) growth rate is the same for the runs C1 and C2. We also observe formation of cell-like structures with unit aspect ratio in the run C2. Figure 14 gives a summary of our Cartesian simulations showing plots of kinetic and magnetic energy versus time. Comparing these results with the corresponding plots for our spherical wedge runs S1 and S7 we observe that the decrease in the large-scale magnetic field is similar to those in the Cartesian domains, if the aspect ratios are chosen similarly. Similar behavior has earlier been seen in simulations in Cartesian domains with aspect ratios not equal to unity (Brandenburg et al. 2002). What is particularly interesting in our case is that, in both Cartesian and spherical coordinates systems, the observed cell structures are persistent, with lifetimes larger than the duration of our longest simulations which, in turn, are longer than the magnetic diffusion time based on L_ϕ (for spherical runs) or L_z (for Cartesian runs). For example, we have checked that in the case of run S7 the cell structures remain unchanged for at least as long as 400 dissipative times, τ_η.

4. CONCLUSION

We have made a detailed numerical study of the effects of changes in the geometrical shape and size of the spherical wedge domains on the growth and saturation of large-scale magnetic fields. We have used direct three-dimensional numerical simulations of helically forced MHD equations using random helical forcing.

For the smallest domain with aspect ratio close to 1, we find dynamo action resulting in magnetic fields on scales larger than the characteristic scale of the forcing. The large-scale magnetic energy grows to exceed the kinetic energy over diffusive timescales, similar to that seen earlier in Cartesian simulations in periodic boxes.

In domains larger in the azimuthal direction, the large-scale magnetic field organizes itself in cell-like structures in the azimuthal direction. The aspect ratio of the individual cells is close to unity. This large-scale pattern in the azimuthal direction has $m = 8$. This is determined by the smallest (radial) scale in the simulations. (As an aside, somewhat similar behavior was found by Moss et al. 1990 in a study of mean-field dynamos.) To encompass such a structure within the computational domain, we have to have $L_\phi \geqslant (\pi/4)r_2$. Further increases in the size of the domain in the azimuthal direction just make the cells repeat themselves, tiling the domain along the azimuthal direction, and thus resulting in very small longitudinally averaged fields for larger domain sizes. We note that this implies that extrapolation of results from Cartesian box simulations with unit aspect ratio to spherical shells can be misleading. We have also studied the effects of increasing the size of the domain in the meridional extent. The resulting large-scale magnetic fields show little qualitative change except for a marginal increase, provided $L_\theta \geqslant (\pi/5)r_2$; see Figure 8. Hence the smallest wedge-shaped domain in which we can expect to observe features of simulations in a full sphere must have $L_\phi = (\pi/4)r_2$ and $L_\theta = (\pi/5)r_2$.

Furthermore, the presence of the cellular structures along the azimuthal direction means that the usual employment of longitudinal averaging loses much information if used as a way to define large-scale magnetic fields. Clearly, a possible alternative is to define the large-scale magnetic field via Fourier transform along the ϕ direction of our domain. A large-scale magnetic energy defined in this fashion results in strong fields of equipartition strength in all the domain sizes we have used. We note here that the large-scale magnetic field defined using Fourier filtering obeys some of the Reynolds rules only approximately. For example, the average of the product of an average and a fluctuation vanishes only for infinite scale separation. This shortcoming may cause some discrepancies between theory and model, which is however beyond the scope of the present paper.

In all our simulations, we find the cellular structures to be long lived with lifetimes longer than the duration of our simulations. This therefore suggests that these structures are not transients. In an attempt to compare with mean-field dynamo models, one must note that the excitation conditions for modes with $m > 2$ are normally much higher than for m below 2, although there is a clear trend for this difference to diminish for thinner shells (Brandenburg et al. 1989). On the other hand, anisotropies of the α effect might significantly change this.

It is important to clarify the similarities and differences between our results and those of previous studies. Forced turbulence simulations have been carried out by Mininni & Montgomery (2006) and Mininni et al. (2007) who also adopted a forcing function in terms of Chandrasekhar–Kendall functions—although not random—and used perfectly conducting boundary conditions. They included the effects of rotation and considered both helical and nonhelical forcings. Their computational domain is a full sphere. They considered laminar flow patterns and found large-scale magnetic fields to be generated, but the energy contained in the large-scale component is generally small compared to the kinetic energy. Fully turbulent simulations in spherical shells have been studied by Brun et al. (2002, 2004, 2006), and Brown et al. (2007). These flows are subject to rotation and stratification which make them helical. However, the degree of helicity is weak compared to our fully helical forcing functions and a broad range of wavenumbers is being driven, so it is difficult to identify a well-defined energy-carrying scale.

Our simulations show the effects of magnetic helicity conservation (see Figure 4), but the magnetic Reynolds number is still

rather low, so it may be of interest to repeat such simulations at larger magnetic Reynolds numbers. However, it is important to run for sufficiently long times to be able to obtain full saturation. Obviously, such long saturation times are not astrophysically relevant, and earlier work in Cartesian domains gives clear predictions that the constraints from magnetic helicity are alleviated in the presence of shear giving rise to small-scale magnetic helicity fluxes (Brandenburg 2005; Käpylä et al. 2008). Allowing for latitudinal differential shear motions is therefore one of our next objectives.

Dhrubaditya Mitra is supported by the Leverhulme Trust. He and R.T. thank Nordita for hospitality during the program "Turbulence and Dynamos." A.B. and David Moss thank the Astronomy Unit, Queen Mary University of London, for hospitality. Computational resources were granted by UKMHD, QMUL HPC facilities purchased under the SRIF initiative, and the National Supercomputer Centre in Linköping in Sweden.

APPENDIX A

RANDOM HELICAL FORCING IN SPHERICAL COORDINATES

In this Appendix, we briefly describe the helical forcing used in our simulations in spherical wedge domains. We require the helicity of the forcing to be positive at every time-step at every grid point. Furthermore, in order to obtain a turbulent state we use random forcing which is white-in-time. In Cartesian coordinates, this is achieved by using appropriately normalized Beltrami waves (Brandenburg 2001); in the spherical case we need to use the Chandrasekhar–Kendall function (Chandrasekhar & Kendall 1957). Similar forcing functions, although not random, in spherical coordinate systems have also been discussed by Livermore et al. (2007).

To guarantee positive helicity we demand, following Chandrasekhar & Kendall (1957),

$$\boldsymbol{\nabla} \times \boldsymbol{f} = \alpha \boldsymbol{f} \tag{A1}$$

with a positive α at every point in our computational domain. This in turn implies that $\boldsymbol{f}$ should have the form

$$\boldsymbol{\nabla} \times \boldsymbol{\nabla} \times \boldsymbol{f} = \alpha^2 \boldsymbol{f}, \tag{A2}$$

which, using $\boldsymbol{\nabla} \cdot \boldsymbol{f} = 0$, becomes

$$\nabla^2 \boldsymbol{f} + \alpha^2 \boldsymbol{f} = 0. \tag{A3}$$

Clearly, all solutions of this equation are solutions of Equation (A1) but the converse is not true. To find solutions of (A3), consider a scalar function ψ satisfying the Helmholtz equation,

$$\nabla^2 \psi + \alpha^2 \psi = 0, \tag{A4}$$

whose solutions in spherical polar coordinates are obtained in terms of spherical Bessel function and spherical harmonics,

$$\psi = \sum_{l=0}^{\infty} \sum_{m=-l}^{l} z_l(\alpha r) Y_l^m(\theta, \phi) \exp(\mathrm{i}\xi_m), \tag{A5}$$

where

$$z_l(\alpha r) = a_l j_l(\alpha r) + b_l n_l(\alpha r). \tag{A6}$$

Here, j_l and n_l are spherical Bessel functions of the first and second kind, respectively, and a_l and b_l are constants determined by the boundary conditions. A solution of Equation (A1) can then be constructed as the sum

$$\boldsymbol{f} = \mathbf{T} + \mathbf{S}, \tag{A7}$$

where

$$\mathbf{T} = \boldsymbol{\nabla} \times (\mathbf{e}\psi), \qquad \mathbf{S} = \frac{1}{\alpha} \boldsymbol{\nabla} \times \mathbf{T}. \tag{A8}$$

We wish to confine our forcing to certain bands of length scales and also to randomize it. The characteristic scales of the forcing function in the radial, meridional and azimuthal direction are given by α, l, and m, respectively. As to the choice of boundary conditions, we demand that $\boldsymbol{f}$ is zero at the two radial boundaries $r = r_1$ and $r = r_2$. The constants a_l, b_l, and α are then related by

$$a_l j_l(\alpha r_1) + b_l n_l(\alpha r_1) = a_l j_l(\alpha r_2) + b_l n_l(\alpha r_2) = 0. \tag{A9}$$

For a particular choice of l, this transcendental equation has an infinite number of solutions for α and the ratio a_l/b_l. A higher value of α implies more zeros of the function $z_l(\alpha r)$ lies within r_1 and r_2, which in turn implies that the characteristic radial scale of $z_l(\alpha r)$ becomes smaller. Note that we have periodic boundary conditions along the azimuthal direction, hence the nonzero values of m which are possible in our domain depends on the extent of the domain in the azimuthal direction, i.e., $m_{\min} = 2\pi/L_\phi$, e.g., $m_{\min} = 20$ for the run `S1`. In order to mimic turbulence, we force at the intermediate length scales which allows kinetic energy to cascade to smaller scales. Furthermore, we want the forcing to go to zero at the equator. This implies l must be odd. The values of α, l, and m that we use for the run `S1` are given in Table 3. We used the GNU scientific library[5] to compute the Bessel functions and spherical harmonics in our code.

APPENDIX B

THE PENCIL CODE IN SPHERICAL POLAR COORDINATES

The Pencil Code was originally written in Cartesian coordinates. To use it for our simulations of the compressible MHD equations in spherical polar coordinates, it needs to be changed accordingly. In fact, given its modularity, the Pencil Code is well suited to be generalized to any curvilinear coordinate system. We do this by writing the MHD equations in a covariant form by replacing partial derivatives by covariant derivatives. We shall illustrate this method by considering the particular case of spherical coordinates, which is the one relevant to our simulations here. Let us first consider the divergence of a vector field $\boldsymbol{A}$. In Cartesian coordinates using index notation

$$\boldsymbol{\nabla} \cdot \boldsymbol{A} = A_{\alpha,\alpha}, \tag{B1}$$

where a comma denotes partial differentiation. The same operator can be written in any non-Cartesian coordinate system by replacing the partial derivative by the covariant derivative denoted by a semicolon thus

$$A^{\alpha}_{;\beta} \equiv A^{\alpha}, \beta - \Gamma^{\alpha}_{\sigma\beta} A_{\sigma}, \tag{B2}$$

[5] http://www.gnu.org/software/gsl/.

Table 3
Values of α that Satisfy Equation (A9) Used in the Run S1

m	l	α_1	α_2	α_3
20	81	129.011139	135.938721	143.325378
20	83	130.880829	137.703308	144.992371
20	85	132.771484	139.489746	146.681885
20	87	134.682465	141.297455	148.393219
20	89	136.613068	143.125763	150.125793
40	81	129.011139	135.938721	143.325378
40	83	130.880829	137.703308	144.992371
40	85	132.771484	139.489746	146.681885
40	87	134.682465	141.297455	148.393219
40	89	136.613068	143.125763	150.125793
60	91	138.562683	144.974060	151.879028
60	93	140.530670	146.841827	153.652344
60	95	142.516434	148.728455	155.445251
60	97	144.519348	150.633453	157.257141
60	99	146.538788	152.556305	159.087616
80	121	169.644516	174.748535	180.321686
80	123	171.805023	176.847809	182.341858
80	125	173.971619	178.958252	184.375427
80	127	176.143417	181.079208	186.421967
80	129	178.319519	183.209961	188.481140
100	121	169.644516	174.748535	180.321686
100	123	171.805023	176.847809	182.341858
100	125	173.971619	178.958252	184.375427
100	127	176.143417	181.079208	186.421967
100	129	178.319519	183.209961	188.481140

where $\Gamma^{\alpha}_{\sigma\beta}$ are the connection coefficients obtained from the metric corresponding to the coordinates chosen. In the case of spherical coordinates, the metric takes the form

$$g_{\alpha\beta} = \begin{pmatrix} 1 & 0 & 0 \\ 0 & r^{-1} & 0 \\ 0 & 0 & (r\sin\theta)^{-1} \end{pmatrix}. \tag{B3}$$

We shall write the covariant derivatives in the noncoordinate bases, by defining a new triplet of coordinate differentials

$$\mathrm{d}\hat{r} = \mathrm{d}r, \qquad \mathrm{d}\hat{\theta} = r\,\mathrm{d}\theta, \qquad \text{and} \qquad \mathrm{d}\hat{\phi} = r\sin\theta\,\mathrm{d}\phi. \tag{B4}$$

In these bases, the connection coefficients take a particularly simple form

$$\Gamma^{\hat{\theta}}{}_{\hat{r}\hat{\theta}} = \Gamma^{\hat{\phi}}{}_{\hat{r}\hat{\phi}} = -\Gamma^{\hat{r}}{}_{\hat{\theta}\hat{\theta}} = -\Gamma^{\hat{r}}{}_{\hat{\phi}\hat{\phi}} = 1/r, \tag{B5}$$

$$\Gamma^{\hat{\phi}}{}_{\hat{\theta}\hat{\phi}} = -\Gamma^{\hat{\theta}}{}_{\hat{\phi}\hat{\phi}} = \cot\theta/r, \tag{B6}$$

with all other connection coefficients being zero. This simplification makes this noncoordinate basis particularly appealing for numerical simulations. For example, for the divergence of a vector $\boldsymbol{A}$, we obtain

$$\boldsymbol{\nabla}\cdot\boldsymbol{A} = A_{\hat{\alpha};\hat{\alpha}} = A_{\hat{\alpha},\hat{\alpha}} + 2r^{-1}A_{\hat{r}} + r^{-1}\cot\theta\, A_{\hat{\theta}}, \tag{B7}$$

where

$$A_{\hat{\alpha},\hat{\alpha}} = \partial_r A_{\hat{r}} + \frac{1}{r}\partial_\theta A_{\hat{\theta}} + \frac{1}{r\sin\theta}\partial\phi A_{\hat{\phi}}. \tag{B8}$$

Note that in the noncoordinate basis the metric tensor is the Kronecker delta and so the covariant and contravariant components of a tensor are one and the same, hence in the above expression we have not distinguished between them. As in Equation (B7) any vector differential operator in curvilinear coordinate system can be written as the sum of two parts: the first involving the vector operator in the Cartesian form with added scaling factors r^{-1} and $(r\sin\theta)^{-1}$, and the other part involving the connection coefficients. The modular feature of the Pencil Code then plays an important role since the derivatives in Pencil Code are computed in a separate module, and all we need to do to adapt the Pencil Code to any non-Cartesian coordinate system is to change this derivative module by adding the scaling factors corresponding to the coordinate system chosen. The vector operators, e.g., divergence, curl, Laplacian, etc., are then calculated in a different module which uses the derivative module. The parts which depend on the connection coefficients are added to this module. The other minor changes to the code involves coding new boundary conditions and new modules to calculate volume averages. All these changes are now part of the public release of the code.

For completeness, we list here the expressions for the most commonly used vector differential operators in our code. For the curl of a vector field $\boldsymbol{A}$, we have

$$\boldsymbol{\nabla}\times\boldsymbol{A} = \begin{pmatrix} A_{\hat{\phi};\hat{\theta}} - A_{\hat{\theta};\hat{\phi}} \\ A_{\hat{r};\hat{\phi}} - A_{\hat{\phi};\hat{r}} \\ A_{\hat{\theta};\hat{r}} - A_{\hat{r};\hat{\theta}} \end{pmatrix} = \begin{pmatrix} A_{\hat{\phi},\hat{\theta}} - A_{\hat{\theta},\hat{\phi}} \\ A_{\hat{r},\hat{\phi}} - A_{\hat{\phi},\hat{r}} \\ A_{\hat{\theta},\hat{r}} - A_{\hat{r},\hat{\theta}} \end{pmatrix} + \begin{pmatrix} r^{-1}\cot\theta A_{\hat{\phi}} \\ -r^{-1}A_{\hat{\phi}} \\ r^{-1}A_{\hat{\theta}} \end{pmatrix}. \tag{B9}$$

For the advective operator, we obtain

$$\begin{aligned} (\mathbf{u}\cdot\nabla\boldsymbol{A})_{\hat{r}} &= u_{\hat{r}}A_{\hat{r},\hat{r}} + u_{\hat{\theta}}A_{\hat{r},\hat{\theta}} + u_{\hat{\phi}}A_{\hat{r},\hat{\phi}} \\ &\quad - r^{-1}u_{\hat{\theta}}A_{\hat{\theta}} - r^{-1}u_{\hat{\phi}}A_{\hat{\phi}} \\ (\mathbf{u}\cdot\nabla\boldsymbol{A})_{\hat{\theta}} &= u_{\hat{r}}A_{\hat{\theta},\hat{r}} + u_{\hat{\theta}}A_{\hat{\theta},\hat{\theta}} + u_{\hat{\phi}}A_{\hat{\theta},\hat{\phi}} + r^{-1}u_{\hat{\theta}}A_{\hat{r}} \\ &\quad - r^{-1}\cot\theta\, u_{\hat{\phi}}A_{\hat{\phi}} \\ (\mathbf{u}\cdot\nabla\boldsymbol{A})_{\hat{\phi}} &= u_{\hat{r}}A_{\hat{\phi},\hat{r}} + u_{\hat{\theta}}A_{\hat{\phi},\hat{\theta}} + u_{\hat{\phi}}A_{\hat{\phi},\hat{\phi}} \\ &\quad + r^{-1}u_{\hat{\phi}}A_{\hat{r}} + r^{-1}\cot\theta\, u_{\hat{\phi}}A_{\hat{\theta}}. \end{aligned} \tag{B10}$$

To calculate the second-order differential operators, we need the expression for second-order covariant derivative given by

$$\begin{aligned} A_{\hat{\alpha};\hat{\beta}\hat{\gamma}} &= A_{\hat{\alpha};\hat{\beta},\hat{\gamma}} - \Gamma^{\hat{\sigma}}{}_{\hat{\alpha}\hat{\gamma}}\,A_{\hat{\sigma};\hat{\beta}} - \Gamma^{\hat{\sigma}}{}_{\hat{\beta}\hat{\gamma}}\,A_{\hat{\alpha};\hat{\sigma}} \\ &= A_{\hat{\alpha},\hat{\beta}\hat{\gamma}} - \Gamma^{\hat{\sigma}}{}_{\hat{\alpha}\hat{\beta}}\,A_{\hat{\sigma},\hat{\gamma}} - \Gamma^{\hat{\sigma}}{}_{\hat{\alpha}\hat{\beta},\hat{\gamma}}\,A_{\hat{\sigma}} - \Gamma^{\hat{\sigma}}{}_{\hat{\alpha}\hat{\gamma}}\,A_{\hat{\sigma},\hat{\beta}} \\ &\quad + \Gamma^{\hat{\sigma}}{}_{\hat{\alpha}\hat{\gamma}}\Gamma^{\hat{\upsilon}}{}_{\hat{\sigma}\hat{\beta}}\,A_{\hat{\upsilon}} - \Gamma^{\hat{\sigma}}{}_{\hat{\beta}\hat{\gamma}}\,A_{\hat{\alpha},\hat{\sigma}} + \Gamma^{\hat{\sigma}}{}_{\hat{\beta}\hat{\gamma}}\Gamma^{\hat{\upsilon}}{}_{\hat{\alpha}\hat{\sigma}}\,A_{\hat{\upsilon}}. \end{aligned} \tag{B11}$$

For example, the Laplacian of a scalar field Ψ is given by

$$\Delta\Psi = E_{\hat{\beta};\hat{\beta}} = (\partial_{\hat{\beta}}\Psi)_{,\hat{\beta}} + \frac{2}{r}\Psi_{,\hat{r}} + \frac{\cot\theta}{r}\Psi_{,\hat{\theta}}, \tag{B12}$$

and the grad div operator takes the form

$$\boldsymbol{\nabla}\boldsymbol{\nabla}\cdot\boldsymbol{A} = \begin{pmatrix} A_{\hat{\alpha},\hat{\alpha}\hat{r}} + 2r^{-1}\,A_{\hat{r},\hat{r}} + r^{-1}\cot\theta A_{\hat{\theta},\hat{r}} - 2r^{-2}\,A_{\hat{r}} - r^{-2}\cot\theta A_{\hat{\theta}} \\ A_{\hat{\alpha},\hat{\alpha}\hat{\theta}} + 2r^{-1}\,A_{\hat{r},\hat{\theta}} + r^{-1}\cot\theta A_{\hat{\theta},\hat{\theta}} - r^{-2}\sin^{-2}\theta A_{\hat{\theta}} \\ A_{\hat{\alpha},\hat{\alpha}\hat{\phi}} + 2r^{-1}A_{\hat{r},\hat{\phi}} + r^{-1}\cot\theta A_{\hat{\theta},\hat{\phi}} \end{pmatrix}. \tag{B13}$$

REFERENCES

Brandenburg, A. 2001, ApJ, 550, 824
Brandenburg, A. 2005, ApJ, 625, 539

Brandenburg, A., & Dobler, W. 2001, A&A, 369, 329
Brandenburg, A., & Dobler, W. 2002, Comput. Phys. Commun., 147, 471
Brandenburg, A., Dobler, W., & Subramanian, K. 2002, Astron. Nachr., 323, 99
Brandenburg, A., Tuominen, T., & Rädler, K. H. 1989, GAFD, 49, 45
Brown, B. P., Browning, M. K., Brun, A. S., Miesch, M. S., Nelson, N. J., & Toomre, J. 2007, in AIP Conf. Proc. 948, Unsolved Problems in Stellar Physics: A Conference in Honor of Douglas Gough, ed. R. J. Stancliffe et al. (New York: AIP), 271
Browning, M. K. 2008, ApJ, 676, 1262
Brun, A. S., Miesch, M. S., & Toomre, J. 2004, ApJ, 614, 1073
Brun, A. S., Miesch, M., & Toomre, J. 2006, ApJ, 614, 1073
Brun, A. S., & Toomre, J. 2002, ApJ, 570, 865
Chandrasekhar, S., & Kendall, P. 1957, ApJ, 126, 457
Gilman, P. A. 1983, ApJS, 53, 243
Gilman, P. A., & Glatzmaier, G. A. 1981, ApJS, 45, 335
Gilman, P. A., & Miller, J. 1981, ApJS, 46, 211
Glatzmaier, G. A. 1984, J. Comput. Phys., 55, 461
Glatzmaier, G. A. 1985, ApJ, 291, 300
Glatzmaier, G. A., & Gilman, P. A 1982, GAFD, 31, 137
Hughes, D. W., & Proctor, M. R. E. 2008, Phys. Rev. Lett., 102, 044501
Käpylä, P. J., Korpi, M. J., & Brandenburg, A. 2008, A&A, 491, 353
Krause, F., & Steenbeck, M. 1967, Z. Naturforsch., 22a, 671
Livermore, P. W., Hughes, D. W., & Tobias, S. M. 2007, Phys. Fluids, 19, 057101
Miesch, M. S., et al. 2000, ApJ, 532, 593
Mininni, P. D., & Montgomery, D. C. 2006, Phys. Fluids, 18, 116602
Mininni, P. D., Montgomery, D. C., & Turner, L. 2007, New J. Phys., 9, 303
Moss, D., Tuominen, I., & Brandenburg, A. 1990, A&A, 240, 142